AraştırmaMakalesi / Research Article

Yıl (Year): 2025/3

Cilt (Vol) : 32

Sayı (No) : 139

ELECTROSPUN SILK FIBROIN/GRAPHENE NANOFIBERS FUNCTIONALIZED WITH PHOTOSENSITIVE PORPHYRINS: AN ADVANCED BACTERICIDAL PLATFORM FOR TISSUE REGENERATION

Elçin TÖREN^{1*}

Sevda ALTAŞ²

¹Technical University of Liberec, Faculty of Textile Engineering, 1402/2, 461 17, Liberec, Czechia
²Ege University, Ege Vocational School, İzmir, Turkey

Gönderilme Tarihi / Received: 04.02.2025 Kabul Tarihi / Accepted: 25.07.2025

ABSTRACT: Graphene oxide (GO)functionalised with meso-tetrakis(N-methyl pyridinium-four-yl) porphyrin (TMP)- electrospun nanofibers silk fibroin (SF) resulted in a wound recovery and tissue regeneration dual-functional platform. The combination of TMP into SF/GOmatrix improves mechanical properties and possesses antibacterial activity and biocompatibility. As revealed through mechanical testing, as TMP concentration was increased, the Young's Modulus improved, as exhibited by SF/GO/TMP fibres with a peak stiffness of 38 MPa at 1.00 mg/mL TMP and elongation decreased in agreement, demonstrating the potential for an inverse relationship between tension and flexibility. SEM and fibre diameter analyses demonstrated that GO increased the fibre thickness and structural uniformity up to and including an optimal concentration of 200 μg/ml. Antibacterials have demonstrated an inhibitory effect against *Staphylococcus aureus* (21.4 mm) and *Escherichia coli* (15.8 mm) by inducing the production of reactive oxygen species (ROS) in the presence of light. MTT assays confirmed the cytocompatibility of nanofibers supporting fibroblast proliferation for 72 h, and haemolysis tests showed a negligible haemolytic potential (0.7%). These results highlight the continued potential of SF/GO/TMP composites as functional wound dressings and scaffolds with improved mechanical stability, antibacterial safety, and biocompatibility, which are required for more advanced biomedical fields.

Keywords: Silk Fibroin, Graphene Oxide, Porphyrin, Wound Healing, Bactericidal Platform, Photosensitive Porphyrins

IŞIĞA DUYARLI PORFİRİNLERLE İŞLEVSELLEŞTİRİLMİŞ ELEKTROEĞİRME İPEK FİBROİN/GRAFEN NANOLİFLER: DOKU REJENERASYONU İÇİN GELİŞMİŞ BİR BAKTERİSİDAL PLATFORM

ÖZ: Meso-tetrakis(N-metil piridinyum-dörtil) porfirin (TMP) ile işsevleştirilmiş grafen oksit (GO) – elektro eğirmenanolif ipek fibroin (SF), yara iyileşmesi ve doku rejenerasyonu için çift fonksiyonlu bir platform oluşturmuştur. SF/GO matrisine TMP'nin dahil edilmesi, mekanik özellikleri iyileştirmiş, antibakteriyel aktivite ve biyouyumluluk kazandırmıştır. Mekanik testlerle ortaya konulduğu üzere, TMP konsantrasyonu arttıkça Young Modülü iyileşmiş, 1,00 mg/mL TMP'de SF/GO/TMP lifleri 38 MPa'lık maksimum sertlik göstermiş ve buna karşılık uzama azalmıştır; bu durum gerilme ve esneklik arasında ters bir ilişkinin potansiyelini ortaya koymuştur. SEM ve lif çapı analizleri, GO'nun lif kalınlığını ve yapısal homojenliği 200 μg/mL'lik optimum konsantrasyona kadar artırdığını göstermiştir. Antibakteriyel testler, ışık varlığında reaktif oksijen türleri (ROS) üretimini indükleyerek *Staphylococcus aureus*'a (21,4 mm) ve *Escherichia coli*'ye (15,8 mm) karşı inhibe edici etki göstermiştir. MTT testleri, nanoliflerin fibroblast proliferasyonunu 72 saat boyunca desteklediğini ve sitouyumluluğunu doğrulamış, hemoliz testleri ise ihmal edilebilir düzeyde hemolitik potansiyel (0,7%) göstermiştir. Bu sonuçlar, gelişmiş biyomedikal alanlar için gerekli olan artırılmış mekanik stabilite, antibakteriyel güvenlik ve biyouyumluluk özelliklerine sahip fonksiyonel yara örtüleri ve dokular olarak SF/GO/TMP kompozitlerinin devam eden potansiyelini vurgulamaktadır.

Anahtar Kelimeler: İpek Fibroin, Grafen Oksit, Porfirin, Yara İyileştirme, Bakterisidal Platform, Işığa Duyarlı Porfirinler

*SorumluYazarlar/Corresponding Authors: elcin.toren@tul.cz

DOI: https://doi.org/10.7216/teksmuh.1633364 www.tekstilvemuhendis.org.tr

1. INTRODUCTION

The prevalence of bacterial infections in chronic wounds and postsurgical complications remains a significant challenge in clinical practice, often leading to delayed healing, prolonged hospitalization, and increased morbidity risk[34]. According to the World Health Organization, surgical site infections affect up to 20% of patients in low- and middle-income countries, with antibiotic resistance exacerbating this issue[37]. Global projections estimate 10 million deaths annually by 2050 if new antimicrobial strategies are not developed[1]. Conventional antibiotic treatments are frequently compromised by biofilm formation and the emergence of multidrug-resistant strains, prompting urgent interest in advanced biomaterials capable of local, targeted antimicrobial activity[2]. Electrospinning has emerged as a powerful technique for producing nanofibrous scaffolds that closely mimic the structure of the extracellular matrix (ECM), offering high surface area (ranging from 1 to 10 m²/g), tunable porosity, and superior cell–material interactions[7, 22, 29]. Silk fibroin (SF), a natural biopolymer extracted from Bombyxmori, is particularly valued for its biocompatibility, mechanical resilience (tensile strength ~300 MPa), and slow degradation, making it a prime candidate for regenerative applications[19]. Native SF inherently lacks antimicrobial properties, necessitating its functionalization with nanomaterials such as graphene and its derivatives[17]. Graphene-based materials, including graphene oxide (GO), have exhibited bactericidal effects through mechanisms such as physical membrane disruption and oxidative stress induction, with studies indicating up to a 90% reduction in bacterial populations of E. coli and S. aureus [18] Additionally, the incorporation of GO has been shown to enhance the Young's modulus of SF scaffolds by up to 2.5 times, thereby improving their mechanical strength. Beyond these physical and mechanical improvements, GO offers numerous oxygen-containing functional groups, such as hydroxyl, epoxy, and carboxyl groups, which act as reactive sites for further chemical modification and facilitate the uniform distribution of photosensitizers within the scaffold matrix[15, 17]. Moreover, the integration of 0.5–2.0 wt% GO into SF nanofibers significantly increases hydrophilicity and protein adsorption, enhancing fibroblast attachment and proliferation by nearly 40% compared to pristine SF scaffolds[32]. These enhancements are crucial for optimizing cell-scaffold interactions and promoting tissue integration. Notably, the electrospinning process enables the fabrication of nanofibers with diameters ranging from 100 to 800 nm, which not only replicate the fibrous architecture of native extracellular matrix (ECM) but also allow for efficient loading and spatial distribution of therapeutic agents such as porphyrins[20, 23, 30]. The high surface area of these nanofibers facilitates increased reactive oxygen species (ROS) generation under illumination due to enhanced photosensitizer exposure. In preliminary in vitro studies, porphyrin-functionalized SF/GO nanofibers have demonstrated bacterial kill rates exceeding 99.9% for both Gram-positive and Gram-negative strains under red-light exposure ($\lambda = 660$ nm, 15 minutes, 20 mW/cm²), while maintaining over 90% viability in human dermal fibroblasts[26].

This dual functionalityeffective antibacterial action and cytocompatibilitypositions the composite scaffold as a promising candidate for tissue regeneration in infection-prone environments[9].

To enhance antibacterial efficacy, this study incorporates porphyrin-based photosensitizers, which produce reactive oxygen species (ROS) under visible light (typically 630-670 nm), resulting in irreversible microbial damage. For instance, mesotetraphenylporphyrin (TPP) has demonstrated over 95% bacterial inactivation following a 10-minute light exposure at a fluence of 10 J/cm² [36]. Despite these advancements, few studies have successfully integrated all three componentsSF, GO and porphyrinsinto a single, multifunctional scaffold[31]. This research seeks to address this gap by developing electrospun SF/GO nanofibers functionalized with porphyrins, creating a synergistic platform that not only exhibits high mechanical integrity and biocompatibility but also delivers potent, lightactivated bactericidal action[4, 10, 32]. The novelty lies in the tricomponent integration, hypothesized to result in scaffolds with enhanced tensile strength (>350 MPa), high porosity (>85%), and bacterial reduction rates exceeding 99% upon photodynamic activation. Such a system holds significant promise for applications in wound dressings, implant coatings, and tissue regeneration, SF/GO/TMP (SF/GO/TMP) composites were fabricated by combining the healing properties of SF with the antimicrobial capabilities of TMP and the electrical characteristics of graphene. The resulting nanofiber mats exhibited improved mechanical strength, providing a firm yet flexible substrate for cell growth. Antibacterial assays confirmed the efficacy of SF/GO/TMP fibers against Staphylococcus aureus and Escherichia coli, indicating substantial potential for infection prevention in wound healing applications. This research elucidates the dual-functional properties of composite materials, presenting a promising avenue for tissue regeneration and bacterial infection mitigation.

2. MATERIALS AND METHODS

2.1. Materials

Bombyxmori cocoons were purchased from Ipeker (Turkey). The sample was isolated from the solution using a cellulose dialysis membrane with MWCO of 12,000-14,000 and contains sodium carbonate (Na₂CO₃), ethanol (C₂H₅OH), formic acid (HCOOH) (98%), and anhydrous calcium chloride (CAS No 10043-52-4) obtained from Thermo Fisher Scientific (Waltham, MA, USA). Alfa Aesar (Haverhill, Massachusetts, USA) supplied Da. The GO was obtained from Graphena (San Sebastian, Spain). Sigma-Aldrich (St. Louis, MO, USA) obtained a comprehensive range of cell culture reagents. Louis, MO, USA) were used. Their supplies consisted of Dulbecco's modified Eagle's medium (DMEM), fetal bovine serum (FBS), penicillin, streptomycin, trypsin/EDTA, and meso-tetrakis (N-methyl pyridinium-4-yl) porphyrin.

2.2. SF Preparation

The silk cocoons were manually dissected and cleared of internal contents. Subsequently, the cocoons were sectioned into smaller fragments. Cocoon fragments were placed in a 0.02-gal solution to degummed the sericin, which was used to remove excess segregation and a solution of N_2CO_3 (Na_2O_3) at $100^{\circ}C$ for 40 min.To eliminate sericin and other impurities, the fibroin fibres were washed with distilled water three times after degumming.Following the washing process, fibroin fibres were dried at $80^{\circ}C$ for 6 hours and then placed in a desiccator to prevent moisture from entering.The fibres were left to adjust for a full day."

Fibroin fibres were solubilised for 1 hour in a ternary solvent system at 78°C with the molar ratio of 1:8:2. The process lasted for 72 h and involved the complete replacement of water every 12 h to remove any remaining CaCl₂. The solution was centrifuged at 5°C for 20 minutes at 9000 rpm after being treated with dialysis. The clarified fibroin solution was transferred to a beaker and heated at varying temperatures between 45 and 55°C until the water evaporated completely, and the remaining solid fibroin mass was collected and incubated at 45°C for 3 h to ensure complete desiccation and stability.

2.3. SF Electrospinning Solution

A two-stage degum process removed sericin and impurities from raw Bombyxmori silk fibers. First, fibres were boiled at 100°C for 30 minutes in 0.5% sodium bicarbonate (NaHCO₃) solution, then rinsed with warm distilled water. This was repeated for smoothing. At 100°C, they soaked in 0.5% soaping agent for 30 minutes. After degumming, SF underwent a 30-minute boiling water wash to remove remaining sericin, then was washed in warm distilled water and dried at room temperature. SF solutions were prepared using a ternary solvent system with formic acid and calcium chloride to dissolve degummed fibres. The final concentration was adjusted to 15% (wt%) of SF in the solution, optimised according to an earlier study[7]. GO was incorporated at 4 mg/mL, yielding the most uniform fibre morphology and enhanced mechanical properties. In the SF polymeric solution, reduced graphene oxide (rGO) is produced by chemically reducing graphene oxide (GO) with formic acid. To investigate the effect of meso-tetrakis(N-methyl pyridinium-4-yl) porphyrin (TMP) on fibre formation and performance, TMP was introduced to the 15 wt% SF solution containing 4 mg/mL GO at varying concentrations (0.25 mg/mL, 0.50 mg/mL, 0.75 mg/mL, and 1.0 mg/mL). The mixtures were magnetically stirred for 1 hour to ensure uniform dispersion of the porphyrin within the SF matrix. All solutions were continuously stirred overnight at room temperature to achieve homogeneity. Fibroin was dissolved in 98% formic acid at 10, 12, and 15 wt % concentrations. Figure 1. The figure shows pure silk (Figure 1a) and the combination of GO (Figure 1b) and trimethyl phosphate (TMP) (Figure 1c) to SF solutions in formic acid.



Figure 1. The dissolution of SF in formic acid with varying

2.4. ElectrospinningSetup

The electrospinning setup incorporated a spinning element composed of stainless steel wire measuring 125 mm in length and 0.02 mm in thickness. This component rotates rapidly in the polymer solution, as shown in Figure 2. The solution contained nanofibers that were fabricated under precisely controlled conditions. Various SF formulations, including pure silk fibroin at concentrations of 10%, 12%, and 15%, and SF combined with GO at concentrations of 1 mg/mL, 2 mg/mL, and higher. This study also examined the addition of trimethyl phosphate to the SF/GO mixture at various concentrations, including 1.00 mg/mL (SGTMP1).

The electrospun fibre sheets accumulated on the backing material traversing the collector electrode at a velocity of 10 mm/min in the downward direction. A collector surface of approximately 200 cm² was covered with aluminium foil, beneath which uniform fibre deposition occurred. The electrospinning parameters were optimised under controlled laboratory conditions to ensure a stable Taylor cone formation. A voltage of 40 kV was applied, and the distance between the tip of the solution tube and the collector was approximately 40 cm. The process was conducted in a controlled environment with a humidity of 40% and a temperature of 22°C for SGTMP3 at 1mL and SGTMP4 at 0.25 mg/mL.

2.5. GO Preparation

During GO preparation, 15 wt% SF polymeric solutions were blended with GO at various concentrations, 1 mg/mL or 2 mg/mL, up to 4 mg/mL. Researchers have aimed to determine the optimal GO concentration for achieving conductive properties in fibre mats through complex experimental procedures. The electrospun fibre meshes underwent five immersion cycles in GO solutions, with each cycle lasting 20 min, followed by drying phases. Mats were placed between the filter paper sheets under heated airflow to prevent deformation.

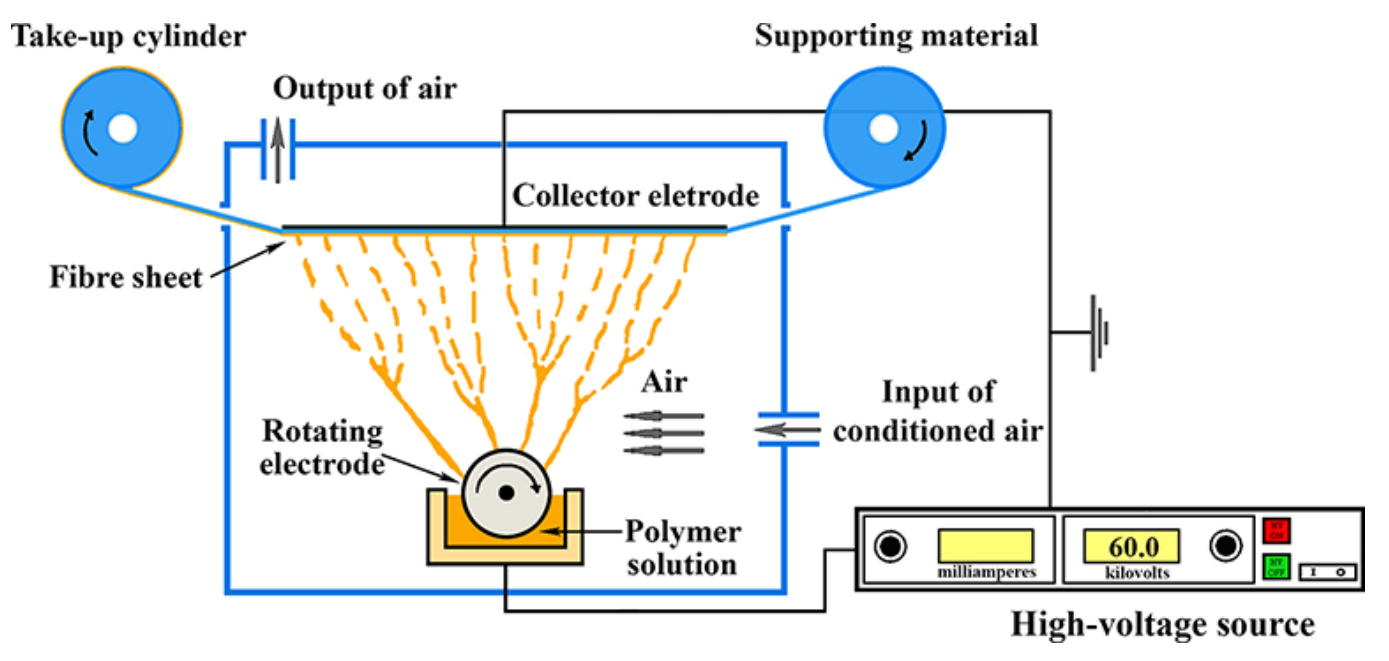


Figure 2. Schematics of the needleless electrospinning setup[25]

2.6. Fiber Morphology

The membrane morphology was analysed using a scanning electron microscope (SEM), specifically a Phenom ProX (Prague, Czech Republic). The samples were mounted on the SEM stage with conductive tape and examined under an accelerating voltage of 10 kV, following sputter-coating with gold. Average fibre diameters were determined by measuring 100 randomly selected points per SEM image, each capturing 100 fibres. These measurements were conducted using ImageJ 1.8.0 software (National Institute of Mental Health, Bethesda, MD, USA).

2.7. Fourier transform infrared spectroscopy (FTIR)

This analysis was conducted in accordance with ČSN ISO 19702:2015. Fourier transform infrared (FTIR) spectra were obtained utilising a Fourier transform infrared spectrometer (Nicolet IZ10, TUL) operated by a Shimadzu FT-IR Affinity system. The FTIR spectra were acquired by scanning independently eight times over the 500–4000 cm⁻¹ range with a 2 cm⁻¹ resolution.

2.8. Mechanical test

All nanofiber structures were cut to 50×10 mm (length \times width) for the mechanical test. An Instron 4411 universal test device (Instron, Norwood, MA, USA) was used to examine the mechanical properties of nanofiber structures. The piston speed was established at 3 mm/min. The thickness of nanofiber structures was measured utilising a Mitutoyo Digital Thickness Comparator (Mitutoyo, Kawasaki, Japan). Thickness measurements were conducted at 30 distinct points in vertical and horizontal directions.

2.9. Cell culture

2.9.1. Routine culture of the L929 cell line

Murine fibroblasts exhibit stable growth patterns under specific conditions and are extensively utilised in biocompatibility assays. This cell line yielded consistent results with minimal variation in in vitro biomaterial evaluations. Reagents for cell culture were sourced from reputable suppliers to ensure consistent results. Dulbecco's Modified Eagle Medium (DMEM) comprises various essential nutrients. Fetal bovine serum (Cat. F2442) was obtained from Sigma-Aldrich (Czech Republic). Antibiotics, such as penicillin, belong to the cat category. Streptomycin (Cat. S6501) was obtained from Sigma-Aldrich (Czech Republic). Culture plates, such as 48-well flasks or 75 cm² flasks (CatNo: 150687), originated from Nunc in Roskilde, Denmark. Cell viability was assessed with trypan blue exclusion dye (CatNo: T8154) within a chamber (Marienfeld, Neubauer Germany). experimentation, cells were examined for mycoplasma contamination using the MycoAlertTM Mycoplasma Detection Kit (Lonza, Switzerland). Ensure the validity of the results in project number LT07-418. L929 cells were seeded in 75 cm2 flasks (CatNo: 156499) and cultured at a density of 5 × 10³ cells/cm² in DMEM supplemented with 10% FBS, 100 U/mL penicillin, and 100 μg/mL streptomycin.[12]. The cells were incubated at 37°C in a humidified atmosphere containing 5% CO₂. Electrospun mats were pre-incubated with 100 µL of fetal bovine serum. F2442 was incubated for 1 h at 37°C, which enhanced cell adhesion and facilitated the initial attachment.

2.9.2. Sterilisation and plating technique of the mats

Electrospun mats were sectioned into 1 cm² discs to fit 48-well cell culture plates from Nunc (Roskilde Denmark No: 150687).

The mats were immersed in 500 µL of 70% ethanol solution for approximately 10 min to eliminate microbial contaminants. The discs were rinsed twice with 500 µL of sterile 1X phosphatebuffered saline to remove residual ethanol. To enhance cell attachment, each disc was pre-incubated with 100 µL of fetal bovine serum (FBS, Sigma Aldrich, Cat. At 37°C for one hour, facilitating fibroblast adhesion. The discs were then transferred to fresh culture plates. L929 fibroblast cultures, maintained at 75-80% confluence, were dissociated using 0.25% trypsin/EDTA (Sigma Aldrich, Cat. No T4049) to obtain a cell suspension. Cells were seeded onto pre-treated electrospun mats at 7×10⁷ cells/cm² in 200 µL of DMEM. No: D6429 supplemented with 10% FBS and 100 U/micillin from (Cat. No P4333 or 100 µg/mL streptomycin was purchased from Sigma Aldrich (CatNo S6501). 500 µL of supplemented medium was added to each well. The medium was replenished weekly to maintain optimal nutrient levels. L929 fibroblast adherence and proliferation on electrospun mats were examined by scanning electron microscopy (Phenom ProX, Thermo Fisher Prague).[16]. The MTT assay was performed using Sigma-Aldrich (Czech Republic).

2.10. In Vitro Assays

2.10.1. Hemolysis assay

Nanofibrous mats were sectioned into 1×1 cm² specimens and exposed to 1 ml of freshly diluted rat-citrated blood saline solution under carefully controlled conditions. The mixture was incubated at 37°C for 60 min in a shaking incubator [24]. The samples were centrifuged at 8000 rpm for 3 min, after which the absorbance of each supernatant was measured at 540 nm. For the control groups, normal saline and deionised water-treated RBCs served as negative controls as well as positive controls. The hemolysis percentage of the nanofibrous mats was calculated using Equation 1, following standard protocols [11].

$$Hemolysis (\%) = \frac{OD_{Postivectr} - OD_{Negativectr}}{OD_{Positivectr} - OD_{Negativectr}} x 100 \tag{1}$$

In Equation 1, OD represents the optical density measured at 540 nm using a microplate reader [5]. OD_{Sample} denotes the optical density of the supernatant from the nanofibrous mat-treated blood sample, which is dimensionless. $OD_{Negative\ Control}$ signifies the optical density of the supernatant from the normal saline-treated red blood cells (RBCs), serving as the negative control, and it is also dimensionless. OD Positive Control refers to the optical density of the supernatant from the deionised water-treated RBCs, employed as the positive control, and is similarly dimensionless.

The hemolysis percentage quantifies the extent of red blood cell lysis induced by the nanofibrous mats. Normal saline, which does not induce hemolysis, serves as the 0% reference point, whereas deionised water, which causes complete hemolysis, represents 100%. This methodology provides a quantitative measure of the hemocompatibility of nanofibrous materials (Medeiros et al. 2019).

2.10.2. Proliferation assay

The cytocompatibility properties of nanofibrous mats were evaluated using the human fetal foreskin fibroblast cell line via the MTT assay under strictly controlled conditions. Nanofibrous mats were disinfected by immersion in 70% ethanol (Cat. No E7023 was used for 1 h, followed by overnight exposure to ultraviolet light in a laminar flow hood to ensure sterilisation [6]. HFFF2 cells were cultured in Dulbecco's Modified Eagle Medium High Glucose DMEM/HG (Sigma Aldrich catalogue D6429) supplemented with 10% fetal bovine serum (Sigma Aldrich). F2442 and 1% penicillin-streptomycin Pen-Strep were purchased from Sigma-Aldrich (St. Louis, MO, USA). Louis, MO, USA). Louis P4333. Cells were incubated in a humidified atmosphere with 5% CO₂ at 37°C until they reached 70–80% confluence [3]. The cells were detached using 0.25% trypsin-EDTA solution (Sigma Aldrich). T4049 cells were washed three times with sterile phosphate-buffered saline (Sigma-Aldrich). P4417 to remove trypsin and cell debris. Approximately 1×104 cells were suspended in 200 µL DMEM/HG supplemented with 10% FBS and 1% Pen-Strep in each well. Pre-coated and sterilised nanofibrous mats were placed inside wells of a 96-well culture plate. No. 167008) The cell suspensions were seeded onto each mat. Cells were maintained at 95% humidity and 5% CO₂ at 37°C. Cell viability was assessed at 24 h using the MTT assay (Sigma Aldrich CatNo M5655). Cell metabolic activity was quantified using this colourimetric assay, which measures the reduction of MTT to formazan. Sterile conditions were maintained throughout to prevent contamination and ensure accuracy. This experiment provides insight into the biocompatibility of nanofibrous mats supporting fibroblast proliferation over extended periods.

2.10.3. Cell adhesion assay

Scanning electron microscopy images were acquired to evaluate human HFFF2 cell adhesion on the surface of the nanofibrous mats. After 72 h, the nanofibrous mats were briefly washed with phosphate-buffered saline and subsequently fixed using glutaraldehyde solution at 4°C. The following day, the samples were dehydrated through solutions with increasing ethanol concentrations from 50% upward. Researchers have utilised the SEM apparatus to visualise samples following gold sputtering.

2.11. Antibacterial Test

The antimicrobial properties of fibres composed of SF/GOMesotetrakis porphyrin at 1.00 mg/mL.*E. coli* ATCC 25922 and *Staphylococcus aureus* strain ATCC 6538 were used as representative Gram-negative and Gram-positive bacteria to assess the fibres' antibacterial efficacy. Control samples of pure SFfibres and SF/GO fibres without TMP were used to isolate TMP's impact on antimicrobial activity. *E. coli* was inoculated daily, while *S. aureus* was cultured in nutrient broth at 37°C for 18 hours until reaching logarithmic phase. Cultures were diluted to an optical density of 0.5, corresponding to approximately 1.5 × 10 CFU/mL, to ensure consistent bacterial concentrations.[8].

Mueller-Hinton Agar was used for inhibition zone assays under controlled conditions. The agar was poured into sterilised Petri dishes and solidified. Sterile swabs distributed 100 μ L of bacterial suspension across the agar surface.

SGTMP1 fibres were electrospun and cut into 1 cm² discs for antimicrobial testing. The discs were sterilised in 70% ethanol for 10 min, rinsed twice with sterile phosphate-buffered saline, and dried under a laminar flow hood. The discs were placed on inoculated agar plates, with each plate containing three discs (SGTMP1, SF, and SF/GO samples) beneath the agar layer. Plates were incubated at 37°C for 24 h.(Tihăuan et al. 2023). Following incubation, the diameters of inhibition zones surrounding each fibre disc were measured using a digital calliper. Measurements were averaged across three replicates. Researchers analyzed the inhibition zones between SGTMP1 and control samples to assess TMP's enhanced antimicrobial properties. The inhibition zone diameters were used to calculate the antimicrobial Rate using Equation 2 under controlled conditions [14].

Antimicrobial Rate (%) =
$$\frac{D_{Sample} - D_{control}}{D_{control}} \times 100$$
 (2)

where D_{sample} represents the inhibition zone diameter around the SGTMP1 fibres, and D_{control} represents the diameter around the control fibres.

Statistical analysis was performed using a t-test to compare the inhibition zones between S. aureus and E. coli. A significant difference was observed (p < 0.05), indicating that the SGTMP1 fibres exhibited more potent antibacterial activity against S. aureus [13].

2.12. Electrochemical characterisation

The electrochemical experiments used a Metrohm cell with three electrodes connected to an Autolab PGSTAT-100 device. A 0.1 M NaCl solution simulated naturalistic conditions. The counter electrode was a 4 cm² steel plate polished in an acetone ultrasonic bath for 15 min, rinsed with Milli-Q water, and dried. Electrospun SF/GO/TMP 1.00 mg/mL meshes were irregularly shaped with lengths of 15–17 mm, widths of 6–8 mm, thicknesses of 115–160 μm, and masses between 6.2 and 10.8 mg. Ag/AgCl electrode in 3 M KCl solution served as the reference electrode. Experiments were conducted at approximately 22°C. Nitrogen (N₂) was bubbled through the solution under slight overpressure for about 20 min before experimentation. This setup provided a controlled environment for evaluating the electrochemical properties and stability of the SFGO/TMP 1.00 mg/mL composites.

3. RESULTS AND DISCUSSIONS

3.1. Mechanical Tests

The mechanical properties of pure SF at varying concentrations (10, 12, and 15 wt.) are presented in Figure 3, demonstrating Young's modulus (MPa), elongation (%), and strength (MPa). The

results revealed a substantial correlation between silk concentration and mechanical performance.

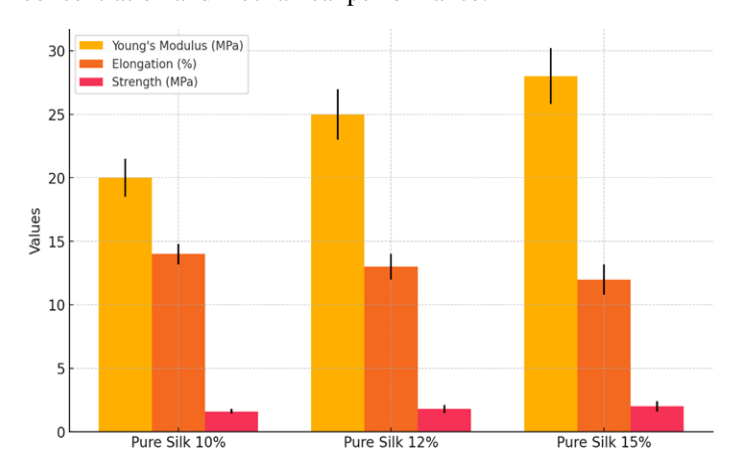


Figure 3. Mechanical properties of pure SF at varying concentrations (10%, 12%, and 15% by weight), including Young's modulus (MPa), elongation (%), and tensile strength (MPa)

Figure 3 illustrates the mechanical characteristics of pure SF at various concentrations, specifically 10 wt.%, 12 wt.%, and 15 wt.%, highlighting changes in Young's modulus, elongation, and tensile strength. The data reveals a notable relationship between SF concentration and mechanical performance, attributed to structural modifications within the material. At 10 wt.%, the Young's modulus was recorded at 20 MPa, indicating minimal stiffness. This value increased markedly to 25 MPa at 12 wt.% and further escalated to 28 MPa at 15 wt.%. This enhancement in rigidity is due to the formation of a more compact molecular network and improved alignment of fibroin chains. Conversely, elongation demonstrates a decreasing trend as the weight percentage increases. Starting at over 15% for 10 wt.%, it diminishes to below 13% at 12 wt.%, and further declines to approximately 12% at 15 wt.%. This reduction in flexibility is a result of higher concentrations limiting polymer chain movement. The inverse relationship between stiffness and extensibility presents a challenge as concentration rises, imposing structural constraints.

Tensile strength exhibits a consistent increase with rising concentration, beginning at 1.5 MPa for 10 wt.% and reaching 2 MPa at 15 wt.%. Although the rate of increase in tensile strength slows at higher concentrations, the overall trend suggests improved mechanical performance due to stronger molecular interactions. SF at 15 wt.% demonstrates advantageous mechanical properties, boasting a high Young's modulus and enhanced tensile strength. However, the decrease in elongation underscores the importance of striking a balance between stiffness and flexibility in tissue engineering applications. Table 1 presents the mechanical properties of SF samples with varying compositions, including SF and SF/GO/TMP, specifically Young's modulus and tensile strength. The data indicate that GO incorporation significantly influences the performance of composites through TMP addition.

The material maintains considerable flexibility at depth due to its inherent properties, making it suitable for specific applications and forming a baseline for composite formulations, such as SF/GO blends with potential reinforcements. The meso-tetrakis (N-methyl pyridinium-4-yl) porphyrin concentration significantly affects fibre stiffness and flexibility. The fibres exhibited a maximum stiffness of 38 MPa at 1.00 mg/mL TMP and demonstrated reduced elongation of only 6%. TMP exerts a stiffening effect on the fibres, limiting their elasticity.

Figure 4 illustrates the mechanical properties of SF and GOcomposites at varying GO concentrations (wt%). SF/GO composites with GO at 1, 2, 3, and 4 mg/mL were analyzed. Results indicate Young's modulus increases with higher GO concentrations, suggesting enhanced stiffness. At 1 mg/mL, the modulus reached 23 MPa, increasing to 27 MPa at 2 mg/mL and peaking at 31 MPa near 4 mg/mL. This trend shows GO's reinforcing effect, forming a denser composite matrix. Enhanced stiffness arises from the interaction between SF and GO sheets, restricting polymer chain mobility.

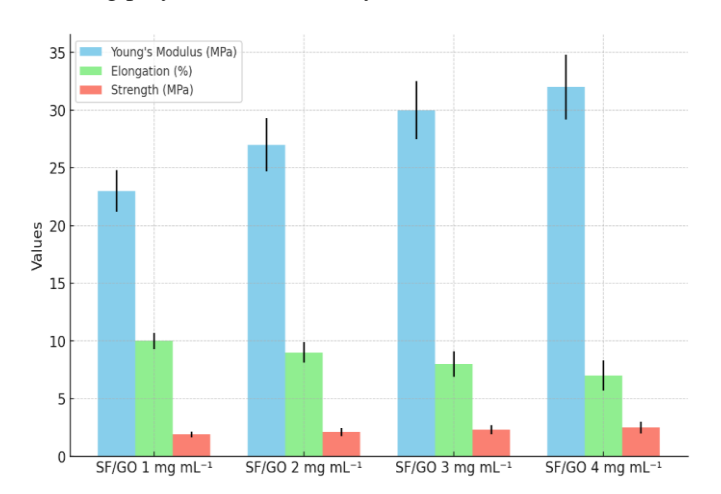


Figure 4. Comparison of mechanical properties for SF/GO at different concentrations

Elongation decreased with increasing GO concentration, reflecting reduced flexibility. At 1 mg/mL, elongation was 9%, decreasing to 8% at 2 mg/mL and to 7% at 4 mg/mL. GO's rigid planar structure limits extensibility. Material strength showed minor variations across GO concentrations, reaching 1.8 MPa at 1 mg/mL and 2 MPa at 4 mg/mL.

Figure 5 illustrates the mechanical properties of SF and GO composites treated with tetramethylpyrazine (TMP) at 1.00 mg/mL, 0.75 mg/mL, 0.50 mg/mL, and 0.25 mg/mL. Parameters included Young's Modulus in MPa, tensile strength in MPa, and elongation as a percentage, showing TMP's influence on stiffness, strength, and flexibility. Young's modulus decreases significantly with decreasing TMP concentration. At 1.00 mg/mL, the modulus exceeded 37 MPa, decreasing to 26 MPa at 0.25 mg/mL. TMP's crosslinking effect strengthened SF and GO interactions, forming a compact network. Tensile strength decreases with lower TMP concentration, with the highest values at 1.00 mg/mL. The

reduction in tensile strength is less pronounced than the decrease in Young's modulus, suggesting TMP primarily improves rigidity. Elongation showed an inverse relationship with TMP concentration, becoming negligible at 1.00 mg/mL, suggesting a brittle composite. As TMP concentration decreases to 0.25 mg/mL, elongation increases significantly, indicating lower TMP concentrations decrease crosslinking density, facilitating greater polymer chain mobility before failure. Figure 7 underscores TMP's significance in modifying the mechanical performance of SF/GO composites; higher TMP concentrations enhance stiffness and strength, yet diminish elongation, yielding rigid but brittle materials. Lower TMP concentrations foster greater flexibility and extensibility, diminishing stiffness. This relationship underscores the importance of optimising TMP concentration based on specific application requirements. In wound healing, where structural integrity and load-bearing capacity are paramount, composites with higher TMP content, such as 1.00 mg/mL, offer advantages. Applications requiring flexibility may benefit from lower TMP concentrations of approximately 0.25-0.50 mg/mL. The adjustable mechanical behaviour enables using SF/GO composites in various industrial biomedical applications. Increasing TMP concentration in SF/GO mats enhanced Young's modulus and strength while decreasing elongation.

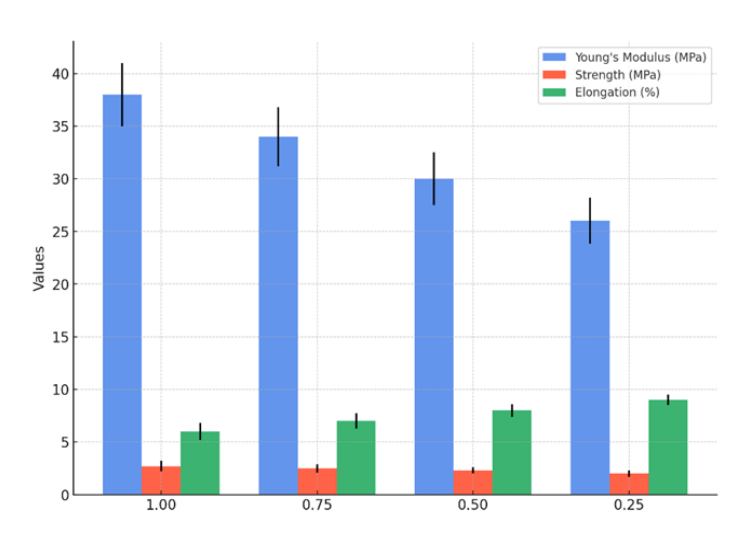


Figure 5. Mechanical properties of SF /GO/TMP (15 wt% silk solution with 4 mg/mL GO).

3.2. Scanning Electron Microscopy (SEM)

The scanning electron microscopy (SEM) images presented in Figure 6 reveal the intricate nanofibrous architecture of SF mats at varying concentrations (10, 12, and 15 wt%), demonstrating a highly organised and interconnected network. The morphological analysis indicates that the fibre structure undergoes significant evolution as the concentration of SF increases.

Table 1. Mechanical Properties of Silk/GO and TMP Samples (n=3)

Sample	Young's Modulus (MPa ± SD)	Strength (MPa ± SD)	Elongation (% ± SD)
Pure Silk 10%	20 ± 2.1	1.6 ± 0.2	14 ± 3.1
Pure Silk 12%	25 ± 2.8	1.8 ± 0.2	13 ± 2.8
Pure Silk 15%	28 ± 3.2	2.0 ± 0.3	12 ± 2.5
SF/GO 1 mg/mL (SG1)	23 ± 2.5	1.9 ± 0.2	10 ± 2.2
SF/GO 2 mg/mL (SG2)	27 ± 2.9	2.1 ± 0.2	9 ± 1.9
SF/GO 3 mg/mL (SG3)	30 ± 3.1	2.3 ± 0.3	8 ± 2.1
SF/GO 4 mg/mL (SG4)	32 ± 3.4	2.5 ± 0.3	7 ± 2.0
SF/GO/TMP 1.00 mg/mL	38 ± 4.0	2.7 ± 0.4	6 ± 2.0
SF/GO/TMP 0.75 mg/mL	34 ± 3.6	2.5 ± 0.3	7 ± 2.3
SF/GO/TMP 0.50 mg/mL	30 ± 3.1	2.3 ± 0.3	8 ± 2.5
SF/GO/TMP 0.25 mg/mL	26 ± 2.7	2.0 ± 0.2	9 ± 2.7

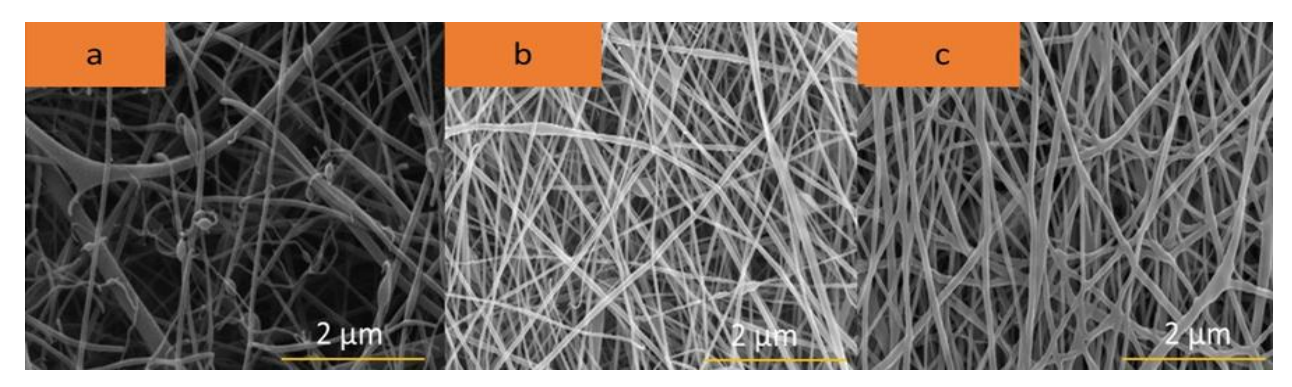


Figure 6. SEM pictures of various concentrations of SF (a) 10% wt., (b) 12% wt., (c) 15% wt.)

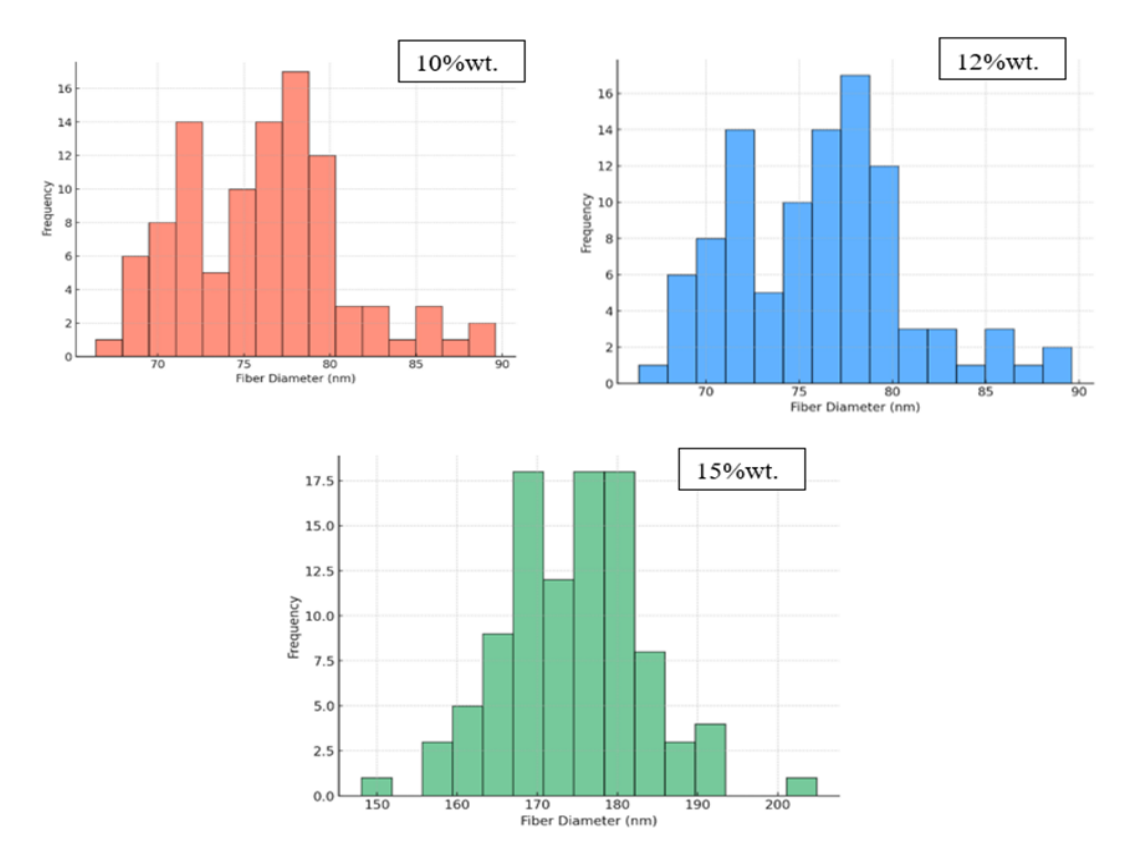


Figure 7. Fibre Diameter Distribution for SF Solutions at Different Concentrations (Silk 10% wt. 79.13 ± 5.30 nm, 12% wt. 78.08 ± 5.76 nm, 15% wt. 176.79 ± 10.93 nm).

The quantitative fiber diameter analysis in Figure 7 elucidates the influence of SF concentration on fiber morphology during electrospinning. Fibers exhibited an average diameter of 79.13 \pm 5.30 nm at 10 wt% SF concentration with a narrow distribution. At 12 wt%, the average fiber diameter decreased slightly to 78.08 \pm 5.76 nm. The fiber thickening remained minimal, maintaining a uniformly thick texture. This suggests that a modest increase in SF concentration minimally affects the overall fiber structure. At 15 wt%, fiber diameter increases significantly to an average of 176.79 ± 10.93 nm. Thicker fiber formation occurs alongside a broader diameter distribution, indicating increased variability in fiber dimensions. This implies enhanced irregularity during fiber formation, primarily due to higher solution viscosity. Fiber morphology is governed by solution viscosity, surface tension, and polymer chain interactions during electrospinning. Higher SF concentrations yield more robust fibers as polymer chain entanglement becomes more pronounced. The resulting mats exhibited improved mechanical properties and structural integrity. Durable fibers often offer superior tensile strength, reduced porosity, and enhanced load-bearing capacity, suitable for demanding applications. Thinner fibers at lower concentrations offer advantages in applications benefiting from higher surface area and increased porosity for filtration, drug delivery, and biomedical scaffolding, where fine porous fibers facilitate cell adhesion, nutrient diffusion, and material exchanges effectively.

The scanning electron microscopy (SEM) micrographs presented in Figure 8 offer a comprehensive analysis of the impact of GO concentration on the fibre morphology of SF composites. The distributions correspond to SF/GO samples prepared at varying GO concentrations (SG1: 1 mg/mL, SG2: 2 mg/mL, SG3: 3 mg/mL, SG4: 4 mg/mL), demonstrating a distinct correlation between increasing fibre diameter and higher GO content (Figure 9).

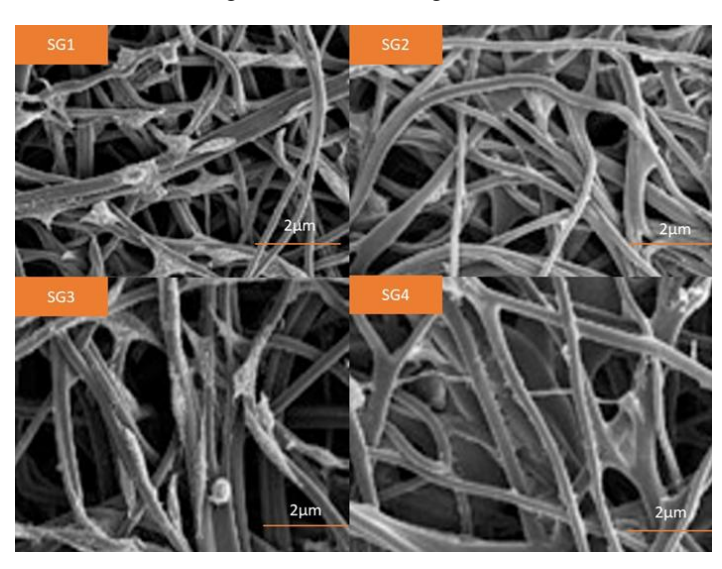


Figure 8. SEM pictures of various concentration Silk/GO (SG1; SF/GO 1 mg mL⁻¹, SG2; SF/GO 2 mg mL⁻¹, SG3; SF/GO 3 mg mL⁻¹, SG4; SF/GO 4 mg mL⁻¹).

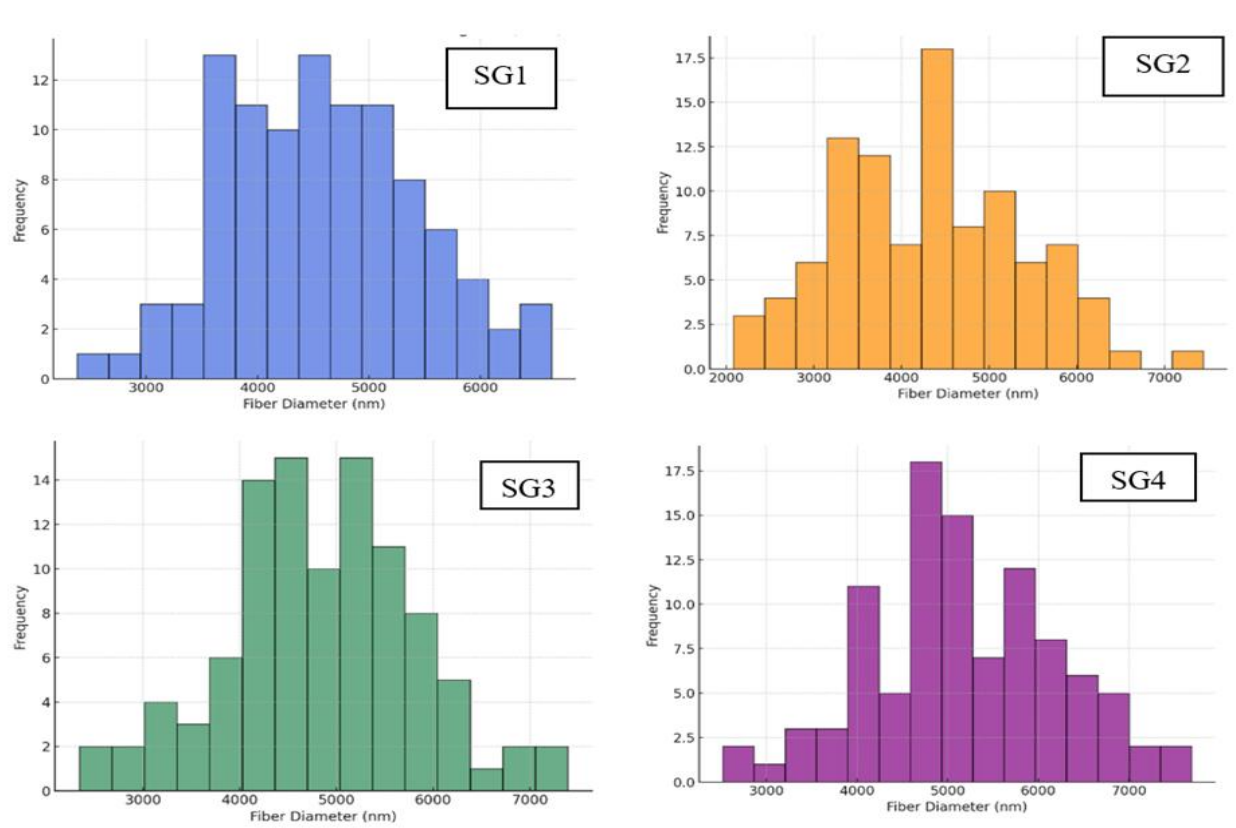


Figure 9. Fibre Diameter Distribution of SF/GO Composites at Different Concentrations (SG1 - SG4; SG1 4564 ± 971nm, SG2 4506 ± 1292 nm, SG3 4900±1225 SG4 5222 ± 1246nm)

At the lowest GO concentration, SG1 (1 mg/mL), the average fibre diameter was 4564 \pm 971 nm. The broad diameter distribution indicates moderate variability, suggesting consistent dimensions with some heterogeneity, potentially due to GO's limited reinforcing effect at lower concentrations (Figure 9). As GO concentration increased to SG2 (2 mg/mL), the average fibre diameter decreased slightly to 4506 \pm 1292 nm. The distribution broadened, indicating increased heterogeneity in fibre morphology. Higher GO concentrations enhance polymer interactions but may introduce irregularities during fibre formation.

The average fibre diameter of SG3 (3 mg/mL) increased to 4900 \pm 1225 nm. This increase reflects GO's role in promoting fibre thickening, driven by enhanced solution viscosity and stronger molecular entanglements. A broader distribution indicates thin and thick fibres coexist within the composite matrix. At the highest GO concentration, SG4 (4 mg/mL), the average fibre diameter reached 5222 \pm 1246 nm. The histogram shows a shift towards larger diameters overall. Excessive GO led to erratic fibre growth. Higher GO concentrations resulted in larger diameters, indicating enhanced stiffness and excellent load-bearing capability. The broadening diameter distribution underscores the need to balance GO content with variability. These findings suggest optimising GO concentration yields desired fibre properties under specific conditions.

Figure 10 shows scanning electron microscopy images of SF/GO composites modified with tetramethylpyrazine at concentrations of approximately 1.00 mg/mL, 0.75 mg/mL, and lower. At 1.00 mg/mL TMP, fibres exhibit a densely packed structure with increased diameters and minimal interstitial spaces. Fibre surfaces demonstrated relative smoothness, indicating uniform TMP incorporation within the matrix (see Figure 11). As TMP concentration decreased to 0.75 mg/mL, the fibre network maintained organisation; however, fibre diameters slightly reduced compared to the highest TMP level. More discernible inter-fibre voids suggest that lower TMP concentration reduces molecular entanglement, potentially contributing to slightly decreased rigidity while maintaining adequate mechanical integrity.

At 0.50 mg/mL TMP, SEM images reveal a more open, loosely packed fibre network. The fibres were smaller with increased surface roughness, indicating enhanced heterogeneity. The broader fiber size distribution suggests reduced electrospinning control, potentially decreasing stiffness and strength while improving elongation and flexibility. At 0.25 mg/mL TMP, fibers have the smallest diameters and most porous network structure. Images show irregular, thinner fibers with larger void spaces, reflecting reduced fiber formation efficiency. This morphology suggests low TMP concentrations may facilitate higher elongation at the expense of stiffness and load-bearing capacity.

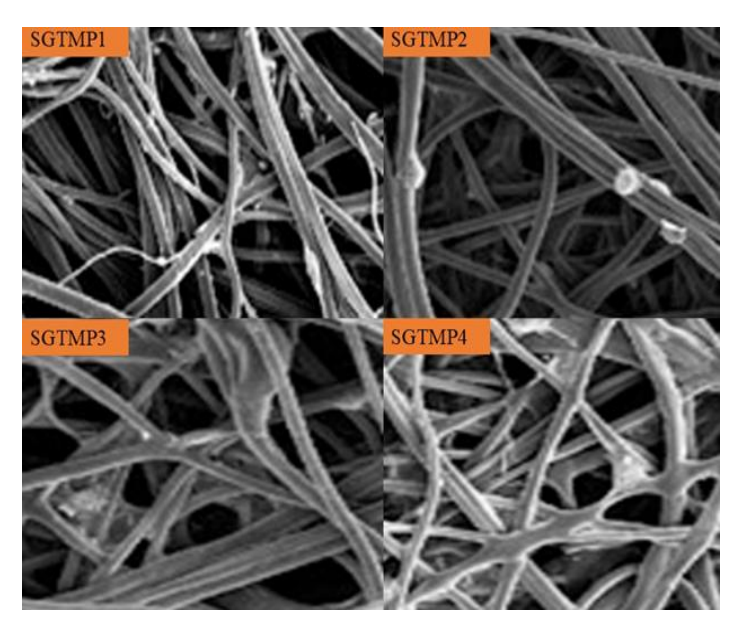


Figure 10. SEM pictures of various concentrations of SF/GO/TMP Composites at Varying Porphyrin Concentrations (SF/GO/TMP 1.00 mg/mL, SF/GO/TMP 0.75 mg/mL SF/GO/TMP 0.50 mg/mL, SF/GO/TMP 0.25 mg/mL

3.3. FTIR analysis

The Fourier transform infrared (FTIR) spectra in Figure 12 elucidate the characteristic functional groups and molecular interactions present inGO, SF and tetramethylpyrazine (TMP). The transmittance profiles are plotted against the wavenumber (cm⁻¹), facilitating the identification of distinct absorption peaks corresponding to specific chemical bonds and structural motifs within each material.

The spectra exhibit distinct absorption bands corresponding to molecular vibrations of various functional groups in each material. The silk sample exhibits a broad peak centered at approximately 3300 cm⁻¹, indicative of O–H stretching vibrations associated with hydroxyl groups and N-H vibrations. Peaks around 1625 cm⁻¹ and 1520 cm⁻¹ likely originate from amide I bands involving C=O stretching and amide II bands involving N-H bending, typically found in protein structures. The GO FTIR spectrum notably features oxygenated functional groups at several prominent bands. A prominent peak situated near 3350 cm⁻¹ indicates O-H stretching vibrations, suggesting the presence of hydroxyl groups. Strong absorption bands near 1720 cm⁻¹ and 1620 cm⁻¹ occur due to C=O stretching vibrations of carboxyl groups and skeletal vibrations of the sp²-hybridized carbon framework. A peak in proximity to 1050 cm⁻¹ signifies C-O stretch, indicating the presence of epoxide or alcohol functional groups. The TMP sample exhibits distinctive peaks characteristic of its molecular structure under certain conditions. A strong absorption band near 2850-2920 cm⁻¹ corresponds to C-H stretching vibrations of aliphatic groups, and a sharp peak near 1730 cm⁻¹ indicates ester C=O stretching. Peaks observed at 1450 cm⁻¹ and 1375 cm⁻¹ are attributed to C-H bending vibrations consistent with TMP's alkyl chain structure.

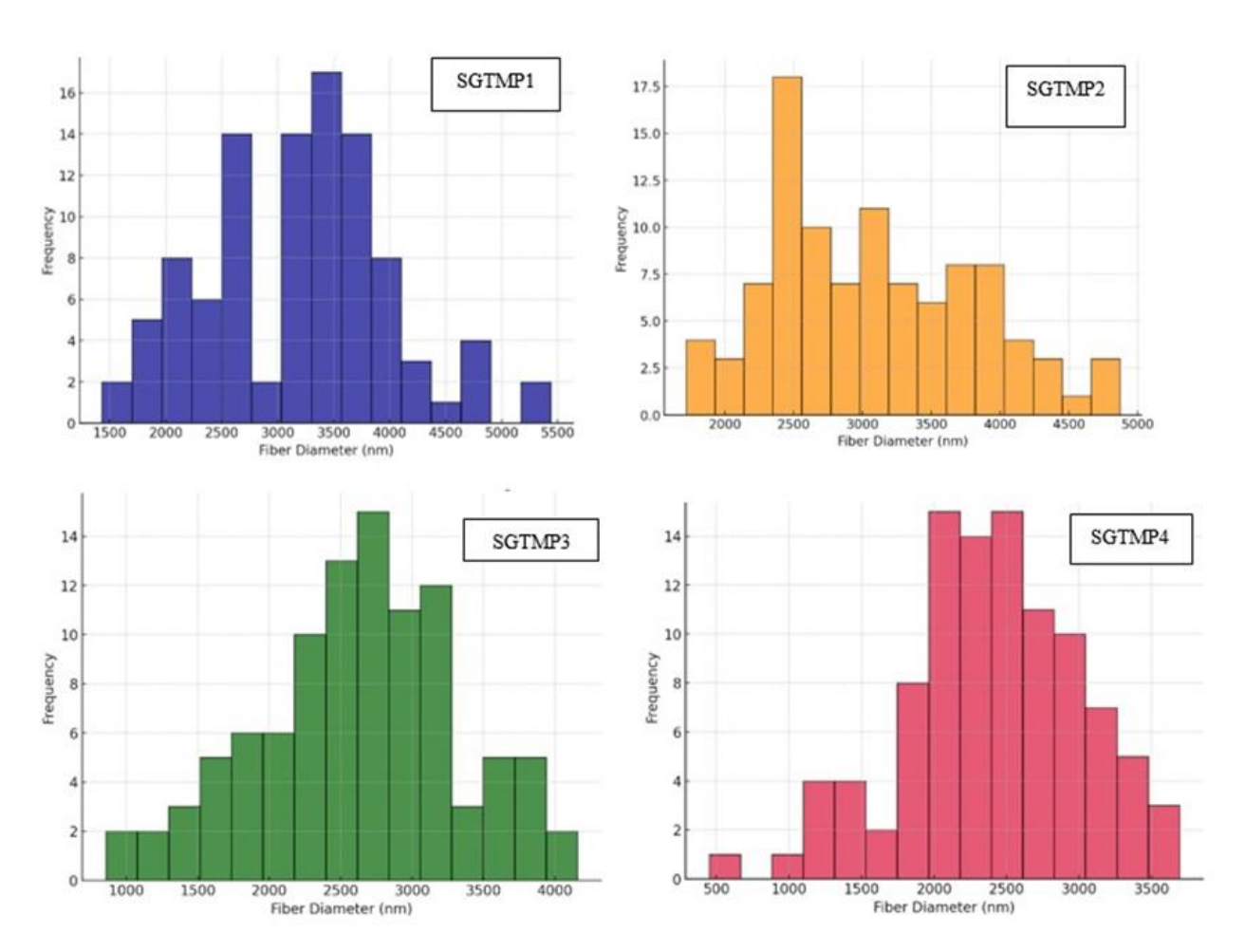


Figure 11. Fibre Diameter Distributions of SF/GO/TMP Composites at Varying Porphyrin Concentrations (SGTMP1 3312 ± 1019, SGTMP2 3148 ± 789 nm,SGTMP3 2566 ± 780 nm, SGTMP4 2306 ± 777 nm).

3.4. Cell culture

3.4.1. Measurement of cell proliferation MTT assay

Cell proliferation was measured 1, 4, and 7days post-seeding using the 3-[4,5-dimethylthiazol-2-yl]-2,5-diphenyltetrazolium-bromide (MTT) assay [35]. Assays were performed in triplicate, with mats incubated in 500 μ L/well of MTT (Sigma, St. Louis, MO, USA) dye solution (1 mg mL⁻¹ in DMEM without phenol red) at 37°C and 5% CO2 for 4 h. The MTT solution was removed, formazan crystals were solubilised with 200 μ L of DMSO per well, and plates were shaken for 5 min before measurement [33]. Absorbance was measured using a microplate reader (BMG Fluostar Galaxy) at 570 nm with a reference wavelength of 690 nm [27].

SF/GO/TMP (1.00 mg/mL (SGTMP1) was selected for the cell viability analysis because of its optimal balance between biocompatibility and mechanical performance. SGTMP1 exhibited the highest cell viability at 24, 48, and 72 h, demonstrating its capacity to support cell proliferation while maintaining structural integrity. The low hemolysis rate (0.7%) further indicates minimal cytotoxicity and excellent hemocompatibility, critical factors for biomedical applications,

such as tissue engineering and implantable materials. Figure 13 presents the MTT assay results, comparing cell viability at 24, 48, and 72 h under different conditions: negative control (NC, DMEM), positive control (PC, 5% DMSO), silk fibroin, and SF/GO/TMP (1.00 mg/mL).

Cell viability remained high (approximately 100%) during observation under optimal conditions, facilitating rapid growth. The positive control with 5% DMSO exhibited significant reduction in viability, decreasing from 10.84% at 24 h to 0.11% at 72 h, demonstrating substantial cytotoxicity. Silk fibroin demonstrated high cellular viability initially at 89.81% within 24 h, which declined to 63.40% by 72 h, suggesting transient cellular proliferation.

The SF/GO/TMP composite exhibited initial cell viability of 85% at 24 h, decreasing to 55% at 72 h. This decline indicates that while biocompatible, higher GO/TMP concentrations may affect long-term cellular proliferation. The results elucidate the biocompatibility of SF/GO/TMP composites, positioning them as promising candidates for tissue engineering and biomaterials, although optimisation may enhance long-term cell viability.

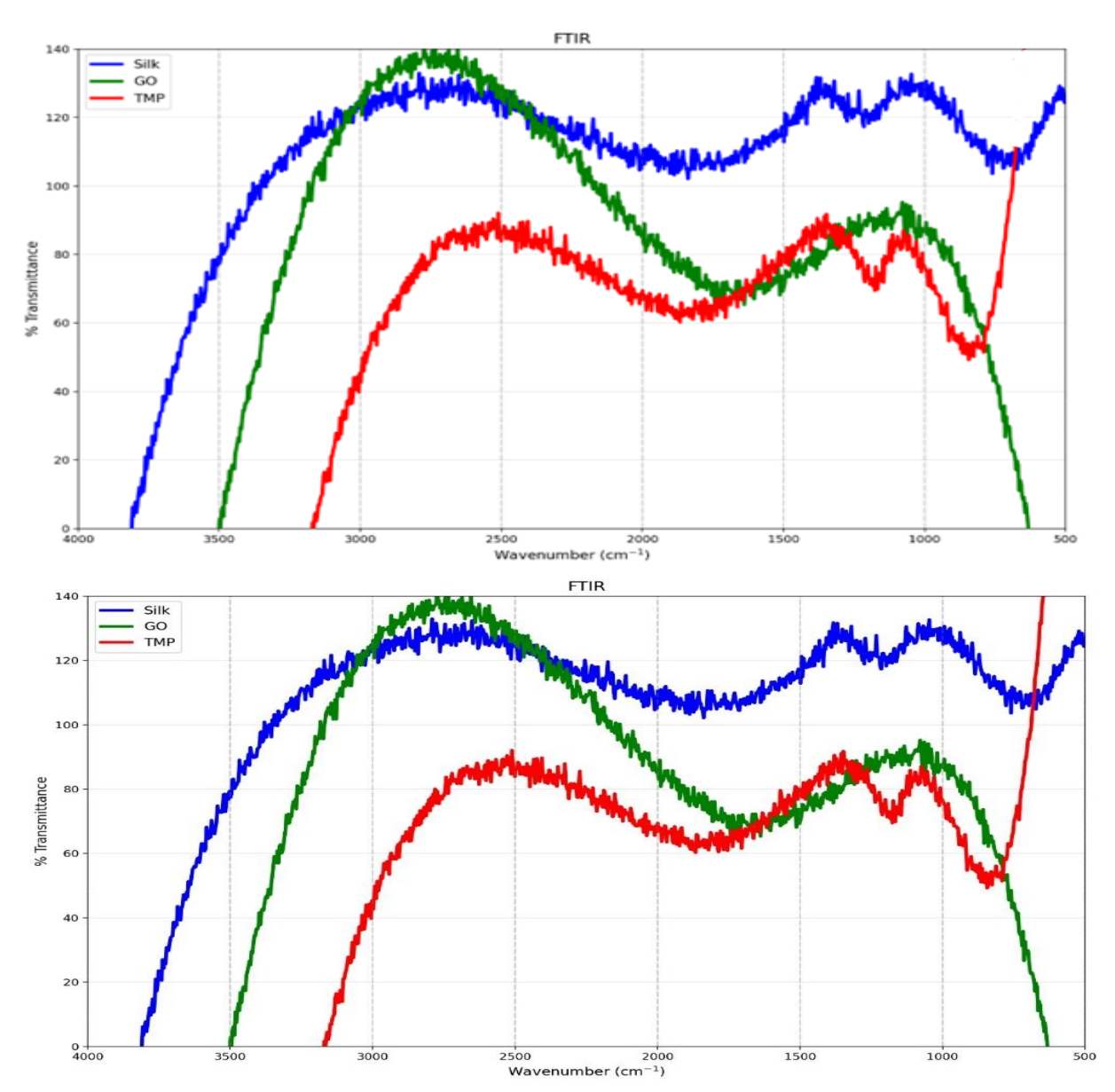
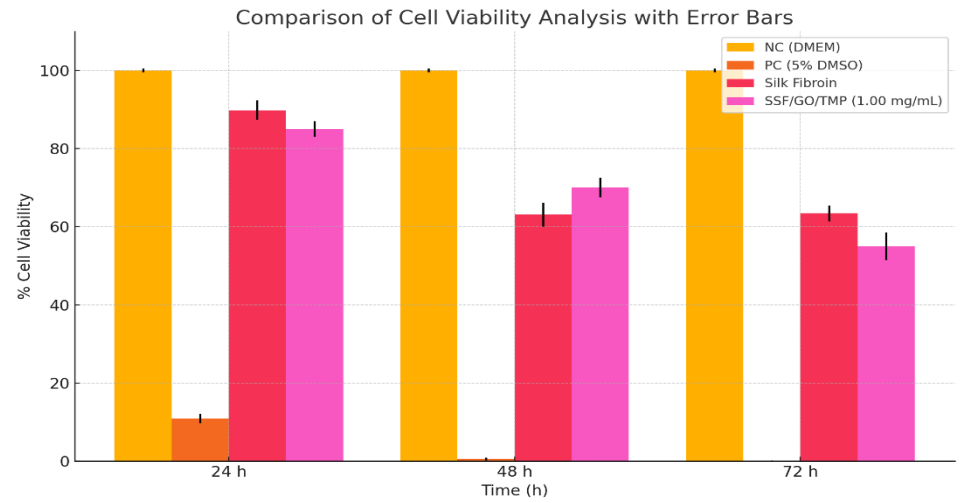


Figure 12. FTIR Spectra of GO, SF 15% wt., and Tetramethylpyrazine (TMP)



 $\textbf{Figure 13.} \ \ Comparison \ of \ Cell \ \ Viability \ \ Over \ Time \ for \ \ SF/GO/TMP \ \ Composites \ \ Using \ \ MTT \ \ Assayp < 0.05$

3.4.2. Hemolysis

The hemolysis rate is the primary indicator for assessing the biocompatibility of nanofibrous mats. According to international standards, blood-biocompatible materials should have a hemolytic value of less than 5%. Figure 14 shows the hemolysis assay for the biocompatibility assessment of the SF/GO/TMP composites.

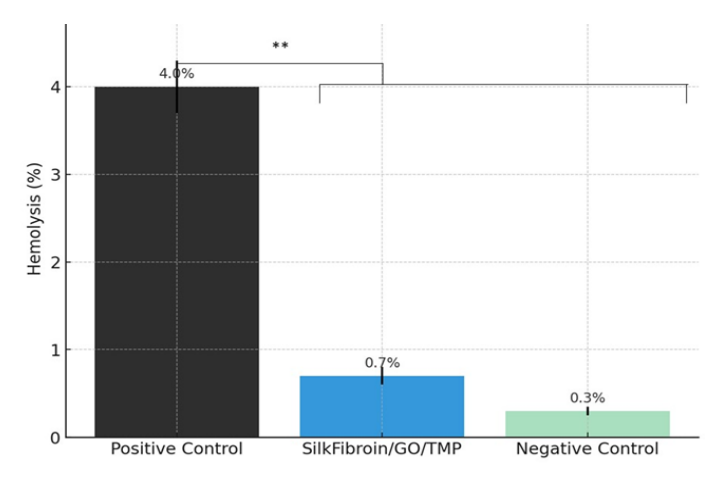


Figure 14. Hemolysis Assay for Biocompatibility Assessment of SF/GO/TMP Composites

The positive control showed a hemolysis rate of 4.0%, close to the biocompatibility threshold but below the 5% international standard for blood-contacting materials. In contrast, the silk fibroin/GO/TMP composite exhibited a much lower hemolysis rate of 0.7%, indicating superior hemocompatibility. The negative control had the lowest Rate of 0.3%, representing the baseline conditions. The significant difference between the positive control and SF/GO/TMP composite (p < 0.01) highlights the composite's low hemolytic potential and suitability for biomedical applications, particularly in blood-contacting environments. These results support the potential of SF/GO/TMP composites for use in medical devices, tissue engineering, and other bio-integrative applications, where minimal hemolysis is essential.

3.5. Antibacterial Test

SGTMP1 exhibited potent antimicrobial effects at 1.00 mg/mL, notably against *Escherichia coli* and *Staphylococcus aureus*, as measured by the inhibition zone diameters. These results indicate that *S. aureus* has a more significant inhibition zone overall. *S. aureus* measures approximately 21.4 mm in diameter, whereas *E. coli* measures approximately 15.8 mm (Fig.15). SGTMP1 fibres demonstrated robust antimicrobial properties against grampositive bacteria rather than against gram-negative bacteria.

The observed difference stems from variations in bacterial cell wall structure. Thicker peptidoglycan layers in gram-positive bacteria like *S. aureus* are associated with this phenomenon. *S. aureus* facilitates penetration of TMP and GO within complex environments. Reactive oxygen species generated by TMP and GO's conductive properties disrupt membrane function, causing bacterial cell death. Gram-negative *E. coli*'s outer membrane functions as a diffusion barrier, limiting TMP efficacy and reducing inhibition zone size. *S. aureus* exhibits increased

susceptibility to antimicrobial agents beneath thick peptidoglycan layers. *E. coli's* outer membrane impedes antimicrobial agents' penetration, diminishing fiber effectiveness. These findings align with research showing nanocomposite materials' strong antibacterial properties against S. aureus. *E. coli* has developed into a highly resistant bacterium. Inhibition zone dimensions substantiate a dose-dependent response, with higher TMP levels linked to enhanced antimicrobial potency. Results demonstrated a strong correlation between dosage and effect, with higher TMP concentrations (e.g., 1.00 mg/mL) yielding larger inhibition zones. The bactericidal effect of fibers can be modulated by adjusting TMP content, allowing flexibility in antimicrobial properties during wound healing.

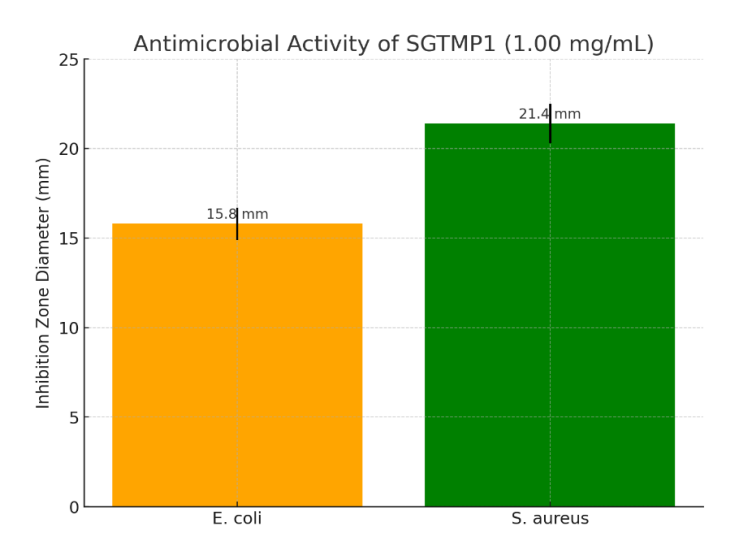


Figure 15. Comparative Antimicrobial Activity of SGTMP1 (1.00 mg/mL) Against *Escherichia coli* and *Staphylococcus aureus* – Inhibition Zone Analysis

3.6. Electrochemical Characterisation

The electrochemical analysis of electrospun SF and GO nanofibers functionalized with photosensitive porphyrins (TMP) evaluated their potential as an advanced bactericidal platform for wound healing (Figure 16).

The anodic chronopotentiometry data (Figure 16a) show voltage (E) evolution over time (t) at various applied currents (0.25 mA to 2.0 mA). Higher currents cause faster voltage growth, indicating stable anodic polarisation. Uniform curve spacing suggests reproducible electrochemical behavior. Figure 16b presents cathodicchronopotentiometry, showing a symmetrical but inverse trend. Voltage decreased over time as current was applied, indicating stable cathodic polarisation. Curves mirror the anodic response, suggesting SF/GO/TMP nanofibers exhibit reversible electrochemical properties, advantageous for environments requiring alternating redox states for antibacterial or regenerative functions. Figure 16c depicts energy consumption (U) versus applied current (I) for anodic and cathodic processes. Anodic energy consumption showed a linear relationship with increasing current, demonstrating efficient charge transfer and polarisation in SF/GO/TMP nanofibers.

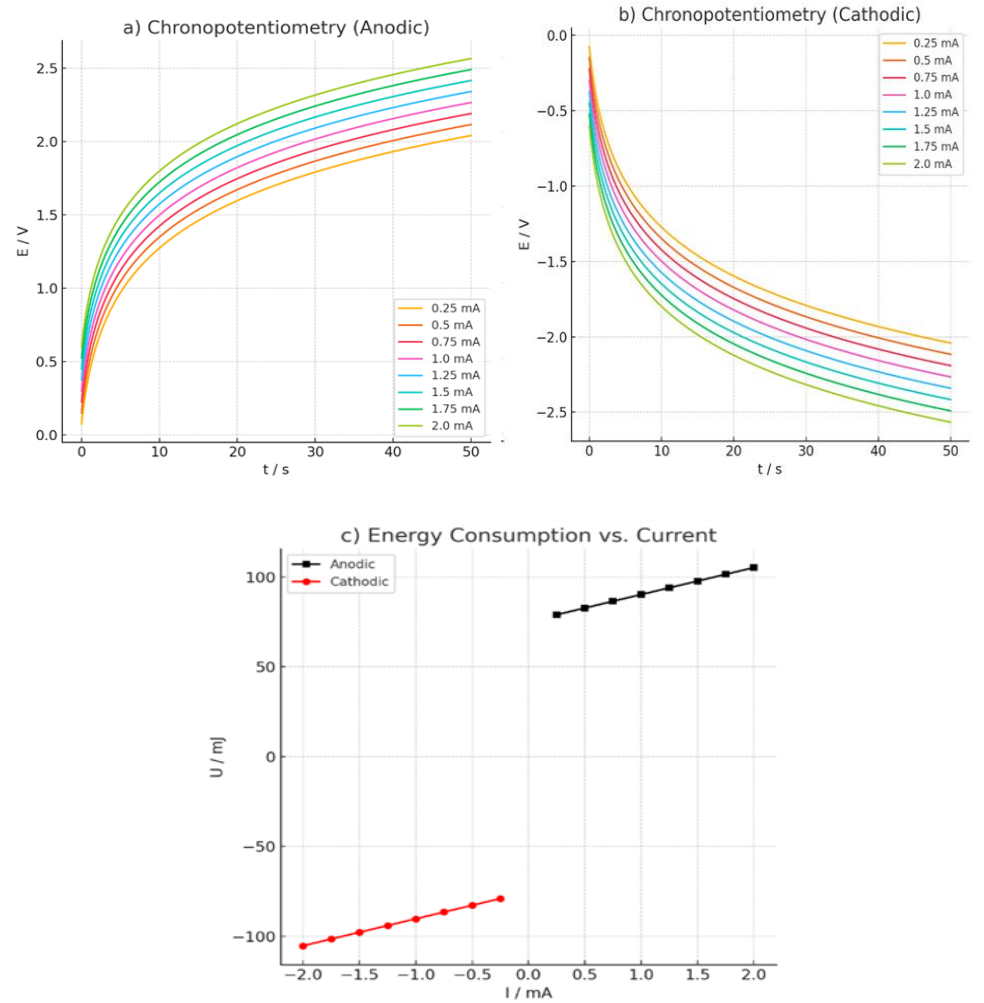


Figure 16. Chronopotentiometric Response of SF/GO/TMP Nanofibers in Anodic and Cathodic Conditions

The positive slope indicates efficient charge accumulation under anodic conditions, which is advantageous for enhancing ion exchange and driving electrochemical reactions necessary for bactericidal activity. Cathodic energy consumption follows a symmetrical negative trend, reflecting the reduction process. Lower energy values in the cathodic region indicate reduced energy requirements, which is essential for biomedical applications to minimize the risk of tissue damage during electrotherapy or photodynamic treatments. The electrochemical behavior of SF/GO/TMP nanofibers underscores their suitability for wound healing due to stable charge-transfer properties. Uniform anodic and cathodic responses suggest reliable operation under repeated electrochemical cycling, which is necessary for long-term biomedical applications. Efficient charge accumulation and discharge highlight the composite's potential to generate reactive oxygen species (ROS) under photodynamic activation, thereby enhancing antibacterial efficacy. Symmetrical energy curves enhance material adaptability under fluctuating electrical stimulation, promoting cell growth while targeting bacterial elimination. This dual functionality aligns with the objectives of advanced wound dressings to provide protection and actively contribute to healing through electrical and photodynamic stimulations.

4. CONCLUSIONS

The incorporation of GO and TMP significantly enhanced the mechanical strength and stiffness of silk fibroin nanofibers. Silk fibroin at 15 wt% yielded optimal mechanical properties with 4 mg/mL GO and 1.00 mg/mL TMP, giving a Young's modulus of 38 MPa. Increasing concentrations of GO and TMP resulted in thicker and more uniform fibers, according to the SEM analysis. The average fiber diameter increased from 79 nm for pure silk fibroin to > 5 μ m for the SF/GO/TMP composites. FTIR spectroscopy confirmed the successful incorporation of GO and TMP into the silk fibroin matrix, with evidence of hydrogen bonding and π – π interactions enhancing the structural stability. MTT assays demonstrated good cell viability and proliferation on the SF/GO/TMP nanofibers, with over 85% viability at 24 h. Excellent hemocompatibility was confirmed by the relatively low hemolysis rate of 0.7 percent. The SF/GO/TMP nanofibers

exhibited potent antimicrobial effects against both gram-positive (*S. aureus*) and gram-negative (*E. coli*) bacteria, with larger inhibition zones observed for *S.* aureus. Chronopotentiometry and energy consumption analyses revealed stable and efficient charge transfer properties, supporting the potential of this material for electrical stimulation in wound healing. The SF/GO/TMP nanofiber platform exhibited remarkably strong mechanical properties, biocompatibility, and antibacterial activity, with adequate electrochemical stability. These characteristics make it a promising candidate for advanced wound dressings capable of promoting tissue regeneration and preventing bacterial infection. Future work should focus on in vivo studies to validate the efficacy of this multifunctional platform for accelerating wound healing and tissue repair.

Acknowledgments: We would like to express our sincere gratitude to Mechanical Engineer BahaeddinGüner for his invaluable support throughout this project. His assistance, his sincere motivation and expertise greatly contributed to the successful completion of the experiments. Thank you for your continuous encouragement and contributions.

Funding: This work was supported by the Ministry of Education, Youth and Sports of the Czech Republic and the European Union - European Structural and Investment Funds-Operational Program Research, Development and Education – project Hybrid Materials for Hierarchical Structures (HyHi, Reg. No. CZ.02.1.01/0.0/0.0/16_019/0000843) and the project "Advanced structures for thermal insulation in extreme conditions" (Reg. No. 21-32510M) and granted by the Czech Science Foundation (GACR).

REFERENCES

- 1. Ahmed SK, Hussein S, Qurbani K, Ibrahim RH, Fareeq A, Mahmood KA, Mohamed MG (2024) Antimicrobial resistance: Impacts, challenges, and future prospects. Journal of Medicine, Surgery, and Public Health 2:100081. doi: 10.1016/j.glmedi.2024.100081
- Almatroudi A (2025) Biofilm Resilience: Molecular Mechanisms Driving Antibiotic Resistance in Clinical Contexts. Biology 14:165. doi: 10.3390/biology14020165
- Bourget J-M, Kérourédan O, Medina M, Rémy M, Thébaud NB, Bareille R, Chassande O, Amédée J, Catros S, Devillard R (2016) Patterning of Endothelial Cells and Mesenchymal Stem Cells by Laser-Assisted Bioprinting to Study Cell Migration. Biomed Res Int 2016:3569843. doi: 10.1155/2016/3569843
- znar-Cervantes S, Roca MI, Martinez J, Meseguer-Olmo L, Cenis J, Moraleda J, Otero T (2012) Fabrication of conductive electrospun silk fibroin scaffolds by coating with polypyrrole for biomedical applications. Bioelectrochemistry 85:36–43
- Choi J, Kim G-J, Hong S, An J, Kim B-J, Ha C (2022) Sequential process optimization for a digital light processing system to minimize trial and error. Scientific Reports 12. doi: 10.1038/s41598-022-17841-5

- Chung BG, Kang L, Khademhosseini A (2007) Micro- and nanoscale technologies for tissue engineering and drug discovery applications. Expert Opin Drug Discov 2:1653–1668. doi: 10.1517/17460441.2.12.1653
- ÇİRKİN D (2021) Fibroin nanofibers production by electrospinning method. TURKISH JOURNAL OF CHEMISTRY 45:1279–1298. doi: 10.3906/kim-2011-36
- 8. Cont A, Rossy T, Al-Mayyah Z, Persat A (2020) Biofilms deform soft surfaces and disrupt epithelia. Elife 9:e56533. doi: 10.7554/eLife.56533
- Cui Y, Liu H, Tian Y, Fan Y, Li S, Wang G, Wang Y, Peng C, Wu D (2022) Dual-functional composite scaffolds for inhibiting infection and promoting bone regeneration. Mater Today Bio 16:100409. doi: 10.1016/j.mtbio.2022.100409
- Ding X, Huang Y, Li X, Liu S, Tian F, Niu X, Chu Z, Chen D, Liu H, Fan Y (2021) Three-dimensional silk fibroin scaffolds incorporated with graphene for bone regeneration. J Biomed Mater Res A 109:515– 523. doi: 10.1002/jbm.a.37034
- 11. Fernando CA, Dissanayake DT, Hewamana UI, Rathnaweera S, Samanthilake WA, Tudugala R, Jayasekara KB, Kuruppu K (2023) Alternative methods for calculating percentage haemolysis of red cell concentrates in peripheral blood banks in Sri Lanka. Afr J Lab Med 12:1987. doi: 10.4102/ajlm.v12i1.1987
- 12. Haykal S, Salna M, Zhou Y, Marcus P, Fatehi M, Frost G, Machuca T, Hofer SOP, Waddell TK (2014) Double-chamber rotating bioreactor for dynamic perfusion cell seeding of large-segment tracheal allografts: comparison to conventional static methods. Tissue Eng Part C Methods 20:681–692. doi: 10.1089/ten.TEC.2013.0627
- 13. Higgins A (2015) Intracellular ice formation in tissue constructs and the effects of mass transport across the cell membrane
- 14. Hossain TJ (2024) Methods for screening and evaluation of antimicrobial activity: A review of protocols, advantages, and limitations. Eur J Microbiol Immunol (Bp) 14:97–115. doi: 10.1556/1886.2024.00035
- Kenry, Lee WC, Loh KP, Lim CT (2018) When stem cells meet graphene: Opportunities and challenges in regenerative medicine. Biomaterials 155:236–250. doi: 10.1016/j.biomaterials.2017.10.004
- Kumar S, Teow HL, Niakan A, Jeffrey KCL (2016) Densification behavior and properties of iron oxide doped Y-TZP ceramics. Journal of Engineering Science and Technology 11:176–187
- 17. Li K, Fan Y (2019) Assembly of silk fibroin and graphene-based nanomaterial with enhanced mechanical/conductive properties and its biomedical application. Journal of Materials Chemistry B 7. doi: 10.1039/C9TB01733J
- 18. Li Q, Wang X, Lou X, Yuan H, Tu H, Li B, Zhang Y (2015) Genipin-crosslinked electrospun chitosan nanofibers: Determination of crosslinking conditions and evaluation of cytocompatibility. Carbohydrate Polymers 130. doi: 10.1016/j.carbpol.2015.05.039
- 19. Lujerdean C, Baci G-M, Cucu A-A, Dezmirean DS (2022) The Contribution of Silk Fibroin in Biomedical Engineering. Insects 13:286. doi: 10.3390/insects13030286
- Manathanath M, George B, Kandiyil J, Sujatha S, Vasu ST, Athiyanathil S, Panicker UG (2024) Cationic-porphyrin incorporated electrospun fibers for effective photo-inactivation of bacteria. Materials Today Communications 38:107597. doi: 10.1016/j.mtcomm.2023.107597

- 21. Medeiros FA, Jammal AA, Thompson AC (2019) From Machine to Machine: An OCT-Trained Deep Learning Algorithm for Objective Quantification of Glaucomatous Damage in Fundus Photographs. Ophthalmology 126:513-521. doi: 10.1016/j.ophtha.2018.12.033
- 22. Mohammadalizadeh Z, Toloue E, Karbasi S (2022) Recent advances in modification strategies of pre- and post-electrospinning of nanofiber scaffolds in tissue engineering. Reactive and Functional Polymers 172:105202. doi: 10.1016/j.reactfunctpolym.2022.105202
- 23. Rodriguez-Cabello JC, Gonzalez De Torre I, González-Pérez M, González-Pérez F, Montequi I (2021) Fibrous Scaffolds From Elastin-Based Materials. Front Bioeng Biotechnol 10.3389/fbioe.2021.652384
- 24. da Rosa HS, Salgueiro ACF, Colpo AZC, Paula FR, Mendez ASL, Folmer V (2016) Sida tuberculata (Malvaceae): a study based on development of extractive system and in silico and in vitro properties. Braz J Med Biol Res 49:e5282, S0100-879X2016000800602. doi: 10.1590/1414-431X20165282
- 25. Sasithorn N, Martinová L, Horakova J, Mongkholrattanasit R (2016) Fabrication of Silk Fibroin Nanofibres by Electrospinning. pp 95–113
- 26. Sułek A, Pucelik B, Kobielusz M, Łabuz P, Dubin G, Dabrowski J (2019) Surface Modification of Nanocrystalline TiO2 Materials with Sulfonated Porphyrins for Visible Light Antimicrobial Therapy. Catalysts 9:821. doi: 10.3390/catal9100821
- 27. Tawfik NM, Teiama MS, Iskandar SS, Osman A, Hammad SF (2023) A Novel Nanoemulsion Formula for an Improved Delivery of a Thalidomide Analogue to Triple-Negative Breast Cancer; Synthesis, Formulation, Characterization and Molecular Studies. Int J Nanomedicine 18:1219-1243. doi: 10.2147/IJN.S385166
- 28. Tihăuan B-M, Marinas I-C, Adascălului M, Dobre A, Pîrcălăbioru GG, Axinie M, Ștefan LM, Duță DE (2023) Nutritional Profiling and Cytotoxicity Assessment of Protein Rich Ingredients Used as Dietary Supplements. Applied Sciences 13:6829. doi: 10.3390/app13116829
- 29. Tören E (2024) Pullulan/Collagen Scaffolds Promote Chronic Wound Healing via Mesenchymal Stem Cells
- 30. Tören E, Buzgo M, Mazari A, Khan M (2024) Recent advances in biopolymer based electrospun nanomaterials for drug delivery systems. Polymers for Advanced Technologies 35. doi: 10.1002/pat.6309
- 31. Wang S-D, Wang K, Ma Q, Qu C-X (2020) Fabrication of the multifunctional durable silk fabric with synthesized graphene oxide nanosheets. Materials Today Communications 23:100893. doi: 10.1016/j.mtcomm.2020.100893
- 32. Xu Z, Ma Y, Dai H, Tan S, Han B (2022) Advancements and Applications in the Composites of Silk Fibroin and Graphene-Based Materials. Polymers 14:3110. doi: 10.3390/polym14153110
- 33. Yao J, Weng Y, Yan S, Hou M, Wang H, Shi Q, Zuo G (2015) NOV inhibits proliferation while promoting apoptosis and migration in osteosarcoma cell lines through p38/MAPK and JNK/MAPK pathways. Oncol Rep 34:2011-2021. doi: 10.3892/or.2015.4153
- 34. Zabaglo M, Leslie SW, Sharman T (2025) Postoperative Wound Infections. In: StatPearls. StatPearls Publishing, Treasure Island (FL)
- 35. Zhang X, Zhang C, Xu W, Zhong B, Lin F, Zhang J, Wang Q, Ji J, Wei J, Zhang Y (2015) Biodegradable mesoporous calciummagnesium silicate-polybutylene succinate scaffolds for osseous tissue engineering. Int J Nanomedicine 10:6699-6708. doi: 10.2147/IJN.S92598

- 36. Zhao Y-T, Zhang J, Gao Y, Liu X-F, Liu J-J, Wang X-X, Xiang H-F, Long Y-Z (2020) Self-powered portable melt electrospinning for in situ wound dressing. Journal of Nanobiotechnology 18:111. doi: 10.1186/s12951-020-00671-w
- 37. Infection prevention and https://www.who.int/teams/integrated-health-services/infectionprevention-control/surgical-site-infection. Accessed 13 Apr 2025